

Article

Soil Texture, Soil Moisture, and Sentinel-1 Backscattering: Towards the Retrieval of Field-Scale Soil Hydrological Properties

Claire Stanyer ¹, Irene Seco-Rizo ¹, Clement Atzberger ²  and Belen Marti-Cardona ^{1,*} 

¹ Faculty of Engineering and Physical Sciences, University of Surrey, Guildford GU2 7XH, UK; cs01075@surrey.ac.uk (C.S.); risecorizo@systra.com (I.S.-R.)

² Mantle-Labs Ltd., London W1J 5RL, UK; clement@mantle-labs.com

* Correspondence: b.marti-cardona@surrey.ac.uk

Abstract: Monitoring soil moisture (SM) on individual crop fields is of great interest for agricultural applications. Synthetic aperture radar (SAR) systems such as Sentinel-1 provide sensitivity to surface SM at a spatial resolution compatible with crop-field monitoring. Different algorithms have been proposed to relate SAR backscattering to SM, yet most overlook soil texture as a modulating factor. This study investigated the influence of soil texture, closely related to soil hydrological properties, on the relationship between Sentinel-1 C-band backscattering and surface SM using extensive data from the agricultural sites of the COSMOS-UK monitoring network. Our results evidenced the semi-empirical first-order relationship between SM and field-averaged VV backscattering, and found that the gradient of their linear regression was indicative of soil texture. For instance, in sandy loam soil the S1 response showed high sensitivity to SM with a change of 1.69% SM per dB; this compared with the lower sensitivity of a clayey soil at a change of 4.81% SM per dB. These findings lay the ground for the retrieval of field-scale soil hydrological properties from backscatter temporal patterns, when used in synergy with rainfall data and process-based soil-moisture models.

Keywords: Sentinel-1; COSMOS; soil moisture; field scale; soil type; soil texture



Academic Editors: Konstantinos X. Soulis and Xianjun Hao

Received: 9 November 2024

Revised: 16 January 2025

Accepted: 29 January 2025

Published: 5 February 2025

Citation: Stanyer, C.; Seco-Rizo, I.; Atzberger, C.; Marti-Cardona, B. Soil Texture, Soil Moisture, and Sentinel-1 Backscattering: Towards the Retrieval of Field-Scale Soil Hydrological Properties. *Remote Sens.* **2025**, *17*, 542. <https://doi.org/10.3390/rs17030542>

Copyright: © 2025 by the authors. Licensee MDPI, Basel, Switzerland. This article is an open access article distributed under the terms and conditions of the Creative Commons Attribution (CC BY) license (<https://creativecommons.org/licenses/by/4.0/>).

1. Introduction

Soil moisture (SM) is a critical climate variable [1], influencing numerous environmental processes including hydrology [2,3], agriculture [4–6], and climate regulation [7–9]. Satellite sensors have become invaluable tools for monitoring surface SM over large areas on a regular basis. As microwaves are particularly sensitive to the dielectric characteristics of observed surfaces, and by extension, to the moisture present [10], they have been used in preference to thermal and optical wavelength measurements [11,12]. Satellite-based SM products include those using passive microwave radiometers such as AMSR-2 [13] and SMOS [11,14], those using active microwave scatterometers such as ASCAT [15] and the Copernicus Global Land Service SSM [16], and the active–passive SMAP product [17]. Passive radiometers are highly sensitive to surface SM but are limited by their coarse spatial resolution, which is insufficient for monitoring moisture conditions at the scale of individual crop fields. Satellite synthetic aperture radar (SAR) data, on the other hand, provide the necessary resolution to capture field-level details [18] but are similarly restricted to surface-level moisture measurements. The Sentinel-1 (S1) satellites from the European Space Agency (ESA)'s Copernicus Programme acquire C-band SAR observations globally at a spatial resolution (10–20 m) and frequency (every 6 days or fewer) compatible with

crop-field moisture monitoring needs [19]. Further, C-band microwaves are minimally affected by cloud cover, allowing observations regardless of meteorological conditions.

A large body of research has related SAR backscattering to SM, independently or in fusion with radiometer data [20–24]. It is well known that the main factors that determine C-band backscattering from agricultural targets, assuming constant observation geometry and polarization, are soil surface roughness [25], vegetation cover [26], and surface dielectric constants [10,27] which is mostly dependent on moisture content. For a field with bare soil and constant surface roughness, the backscattering coefficient (in dB) has been shown to vary linearly with SM [27]. This property has been exploited by widely adopted SAR-based SM retrieval algorithms, on the assumption that, over short periods of time and for the same location (i.e., same soil texture), changes in backscatter will be mainly due to changes in SM (via the dielectric constant) rather than to the variation in other less-fluctuating factors (mainly surface roughness). Notable examples of this approach are TU Wien change detection (TUWCD) [23] and short-term change detection (STCD) [24].

Meanwhile, advances in the remote detection and mapping of precipitation, using remote sensing methods calibrated with rain gauges, have significantly improved accuracy. Widely available satellite-based precipitation datasets include GPM-IMERG [28,29], GPCP-1dd [30], CPC-Global [31], TRMM [32], GSMap [33], PERSIANN-CCS [34], CMORPH [35], MSWEP [36], and CHIRPS [37]. These precipitation datasets, when integrated with process-based models, can simulate infiltration and soil-moisture dynamics in crop fields. However, the global application of such simulation tools in agriculture faces a major challenge: obtaining precise information about soil texture and hydrological properties at the scale of individual fields.

This study lays the groundwork for a novel approach to achieve soil-moisture estimations for individual crop fields. The aim was to retrieve soil infiltration properties—closely related to soil texture—from the temporal behaviour of C-band SAR backscatter, as indicated by previous research [38]. By incorporating these infiltration properties into process-based models, alongside remotely sensed meteorological data, it becomes possible to simulate soil moisture at the root-zone level. In this study, surface soil-moisture data were collected from the COSMOS-UK network, which measures average soil moisture over an area of approximately 200 m in diameter [39]. This footprint provides a better representation of crop field-wide surface SM compared to point-probe readings, as validated in prior work [38]. The analysis revealed that the backscatter-SM relationship was dependent on soil texture across the studied sites, with finer-textured soils exhibiting lower sensitivity compared with sandier soils. These initial findings underscore the potential of this approach and justify further exploration to fully harness its capabilities for field-level soil-moisture mapping and management.

2. Materials and Methods

2.1. Study Sites (*Locations*)

This study focused on 17 sites of the UK COsmic-ray Soil-Moisture Observing System (COSMOS-UK, [39]), referred to in this study as Locations. The COSMOS-UK network has 52 monitoring sites, 17 of which are classified as agricultural and horticultural (A&H). All A&H sites were selected for this investigation as they are likely to have periods of low vegetation after harvesting, during which the C-band return is dominated by the surface backscattering from the soil. Figure 1 indicates the location and name of the study sites. The UK 1 m LiDAR survey flight indicated that all sites have a largely horizontal topography, with maximum slopes lower than 1.3% in all cases [40]. Aerial views of the site, showing consistency within Field-Sectors, are shown later in the study. Of the 17 A&H Locations, 14 are in England, 2 in Scotland and 1 in Northern Ireland.

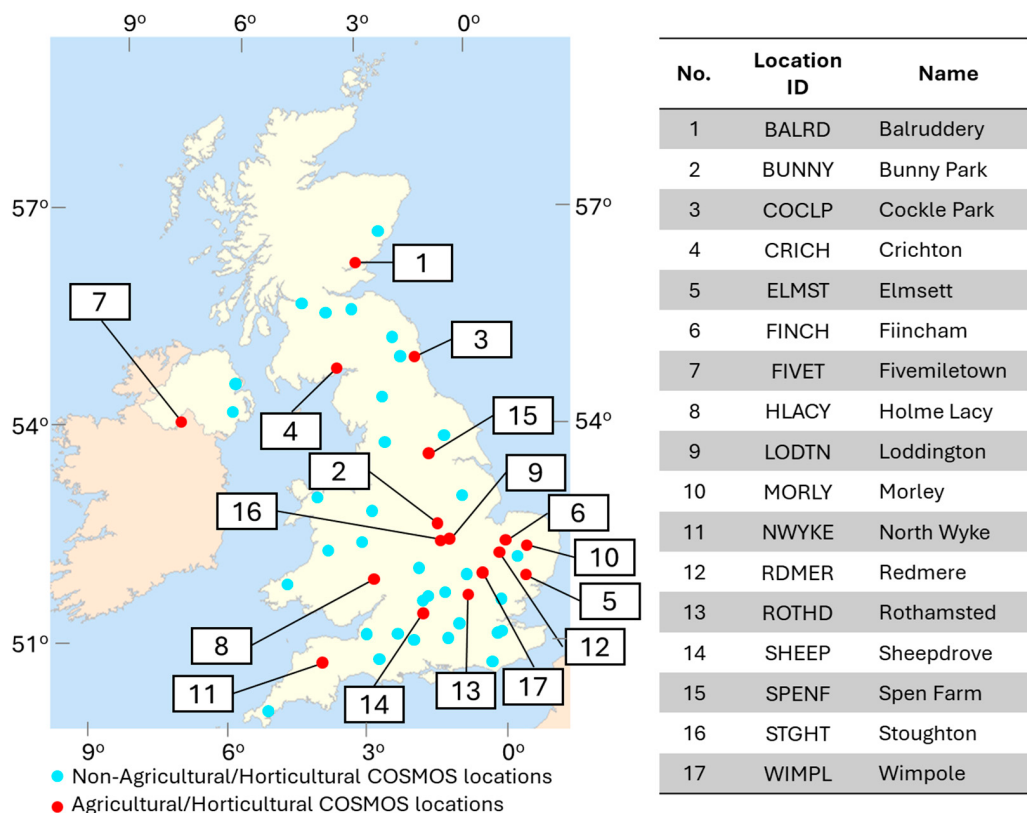


Figure 1. COSMOS-UK agricultural and horticultural Locations and names.

2.2. Datasets

2.2.1. Soil-Moisture Data

Soil moisture (SM) measurements were obtained from COSMOS-UK in the form of volumetric water content (VWC). Established by the Centre for Ecology and Hydrology (CEH) in 2013, the COSMOS-UK network measures soil moisture based on the attenuation of cosmic-ray-induced neutrons by water [41]. The retrieved SM corresponds to an area of 150 to 200 m radius (variable with SM). Thus, these measurements provide an integrative value more representative of the field moisture status than punctual probe readings which are often hindered by large spatial variance [42].

The retrieved SM corresponds to the topsoil layer of approximately 20 cm depth, whilst S1 C-band is sensitive to a finer soil layer of approximately 5 cm. However, studies such as [43] have investigated the relationship between derived C-band SM and COSMOS SM data, showing that satellite-derived soil-moisture products correlate well with cosmic-ray neutron probes such as COSMOS, with such probes being suitable for calibration of remote-sensed SM. Both COSMOS and S1 sensors are sensitive to the average SM over an extended area rather than to point-specific SM. A previous study [38] demonstrated a strong linear relationship between COSMOS and S1 observations, which was notably stronger than the relationship between S1 backscatter and 10 cm-deep point probe readings in the same area. Further, the aim of this study was to investigate the sensitivity of the S1 backscatter-SM gradient to soil texture. As such, the relationship between COSMOS and S1 observations was sufficient for relative comparisons.

COSMOS-UK SM records and metadata were available from 2013 to 2022, at 30 min intervals from the start of observations to 31/12/2019, and at daily intervals from 01/01/2020 to 30/11/2022. The data were cleansed, merged, and averaged, where appropriate, to generate a single SM time series at daily intervals for each Location. Days with missing recordings were omitted. The obtained SM time series were generally complete; therefore, this omission

did not affect the time-series integrity. Figure 2 illustrates the SM records and their temporal availability at the A&H Locations. The overall average surface SM was 41% VWC in the winter (December, January, February) and 29% VWC in the summer (June July, August). The average SM at a Location during the entire period 2013 to 2022 varied between 19% VWC at the BUNNY station and 67% VWC at RDMER, whilst the minimum and maximum recorded SM between 2013 and 2022 were 4% VWC at BUNNY and 75% VWC at RDMER.

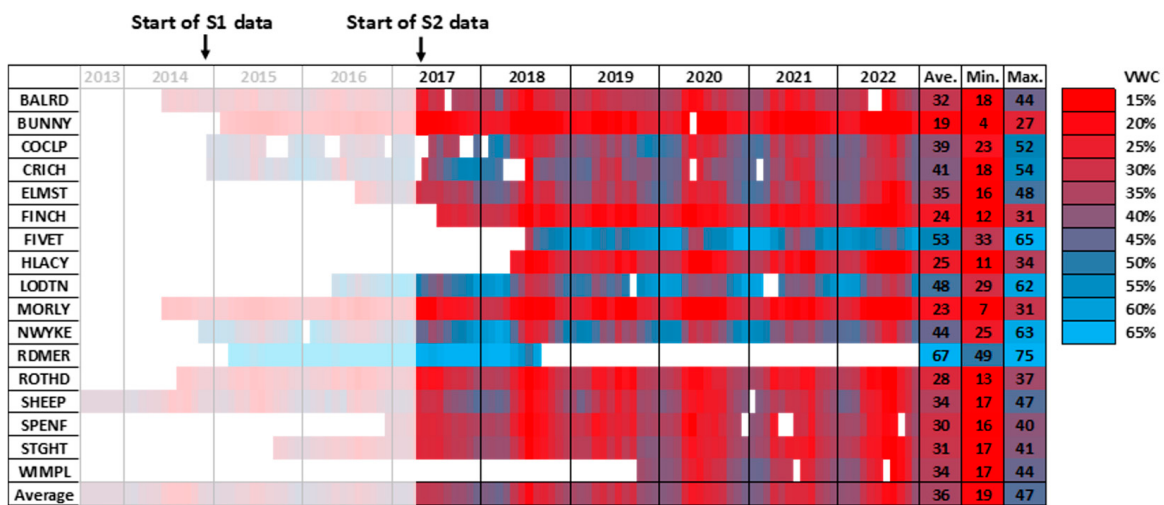


Figure 2. COSMOS-UK SM data: availability periods and VWC variation for the A&H Locations, including minimum, maximum, and average. SM records were used from 2017 onwards, when both S1 and S2 data were available.

2.2.2. Soil Type

The coordinates of the sensor locations, as supplied in the COSMOS-UK metadata, were used to query the UK Soil Observatory (UKSO) Soil Texture database [44]. This provided soil texture descriptions (Table 1) which were used to position each Location in the appropriate sector of the soil texture triangle [45], as shown in Figure 3. The COSMOS description of the Location was used, where necessary, to moderate this placement. Note that the soil texture triangle relates to the mineral content of soil (in % weight) based on particle size. FIVET had no UKSO or COSMOS description, and RDMER was described as “peat” which does not sit on the soil texture triangle.

Table 1. COSMOS-UK agricultural and horticultural Location soil textures.

Location ID	UKSO Soil Type	COSMOS Description
BALRD	Clay loam/sandy loam	Sandy loam
BUNNY	Sand/sandy loam	Loamy sand/sand
COCLP	Clay loam	Loam/clay loam
CRICH	Clay loam/sandy loam	Sandy clay loam
ELMST	Loam/clay loam/chalk	Loam/clay loam
FINCH	Loam/clay loam/chalk	Loam
HLACY	Sandy loam	Loam
LODTN	Clay/clayey loam	Clay
MORLY	Clay/clayey loam/chalk	Clay loam
NWYKE	Clay loam/silty loam	Loam/clay loam
ROTHD	Clay loam	Clay loam
SHEEP	Silty loam/chalk	Loam/chalk
SPENF	Clay loam/silty loam	Loam
STGHT	Loam/clay loam	Loam/clay loam
WIMPL	Clay/clay loam	Clay/clay loam

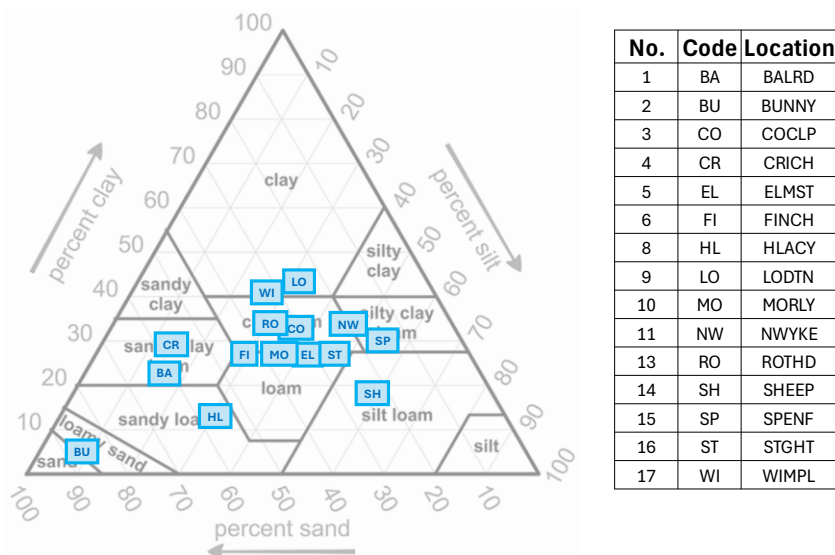


Figure 3. Soil texture at the UK-COSMOS Locations, as described by UKSO and COSMOS-UK.

2.2.3. Copernicus Sentinel Data

This study used all S1A and S1B imagery from April 2014 to November 2022 available for the study sites. The S1 satellites are active systems which emit pulses of C-band electromagnetic radiation at a frequency of 5.405 GHz and record their backscatter from the Earth. The S1 data utilized were acquired in interferometric wide (IW) swath mode and dual polarization vertical–vertical (VV) and vertical–horizontal (VH) [46]. Only the VV polarization data were used due to their higher sensitivity to SM variations [47]. We used the level-1 ground range detected (GRD) product, with a ground spacing distance of 10mx10m. This was accessed through the Google Earth Engine (GEE) platform, image collection COPERNICUS/S1_GRD [46], which had the following Sentinel-1 Toolbox processing applied to derive the backscattering coefficient: orbit file applied, border noise and thermal noise removed, radiometric calibration values applied, terrain correction, and conversion to decibels (dB).

Sentinel-2 bottom-of-atmosphere images were accessed through GEE's image collection COPERNICUS/S2_SR [48]. Sentinel-2 bands 3 and 8, with spatial resolution of 10 m, were used for calculating the normalized difference vegetation index (NDVI) for each study plot. This was done for all cloud-free S2 images of the study sites from April 2017 until 2022.

Figure 2 indicates the temporal availability of S1 and S2 imagery for the study sites relative to the COSMOS SM data.

2.3. Methodology

The overall methodology for this study is illustrated in the flowchart in Figure 4. The steps are described in detail in the following sections.

2.3.1. Delineation of the Study Field-Sectors

The area observed by a COSMOS sensor is known to be around 12 ha [39]. The COSMOS sensors' footprint was therefore approximated in this study by a circle of radius 195 m centered at the sensors' location. Field-Sectors were delineated at the intersection between the COSMOS footprint and the adjacent crop fields. Different Field-Sectors at the same site were labelled as P, Q, R, etc. The delineation excluded a buffer of approximately 10 m to the crop-field borders to avoid features such as hedges or trees. It was desirable that the Field-Sectors had an area of 4 ha or larger, to reduce the deleterious effect of speckle

by averaging the backscattering inside. To this aim, the delineation of some sectors was extended outside the COSMOS footprint, with the assumption that the SM of the field could be considered uniform. A schematic of an example delineation is shown in Figure 5.

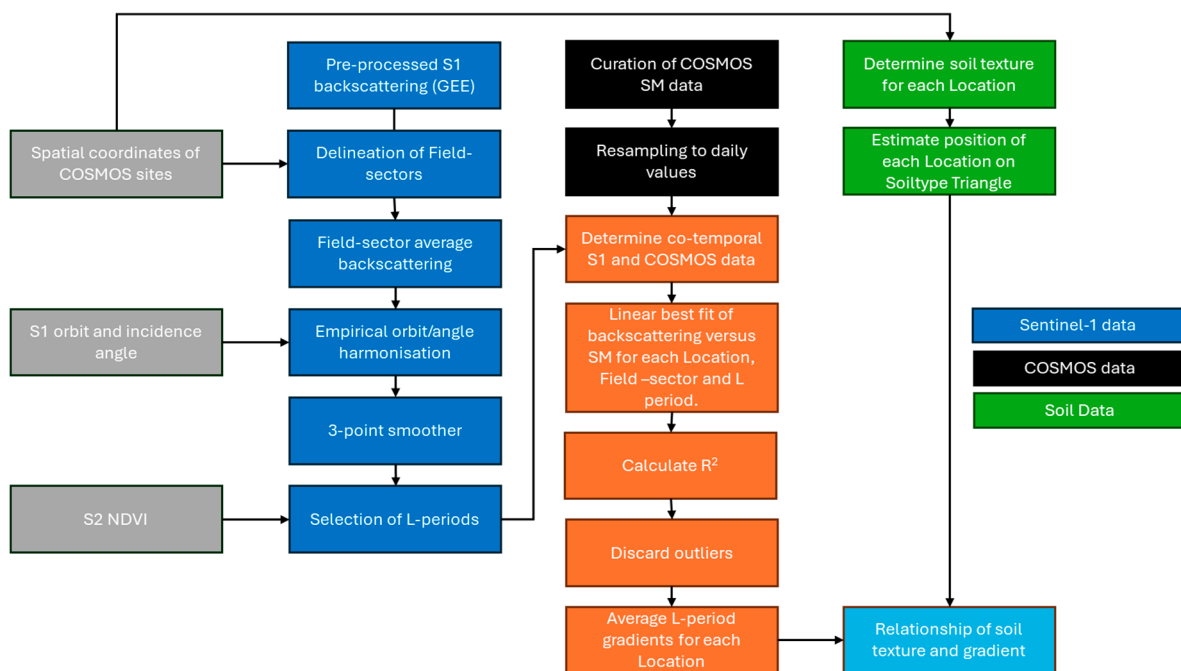


Figure 4. Study methodology overview.

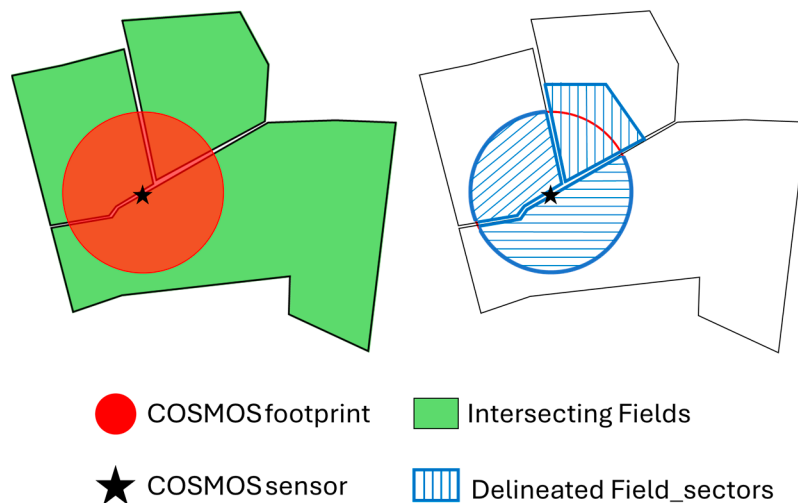


Figure 5. Schematic describing the delineation of Field-Sectors for a sample Location. The COSMOS sensor (black star) is at the center of the COSMOS footprint (red circle), which intersects three fields (green polygons). Varying vegetation levels in the fields mean that three Field-Sectors (blue polygons) needed to be considered independently.

Figure 6 shows the Field-Sectors associated with each Location (COSMOS sensor site).

The average area of the 40 delineated Field-Sectors was 4.88 hectares, ranging from RDMER_P at 11.52 hectares to WIMPL_R at 4.03 hectares, with the exception of FIVET_(P, Q, R, S) being atypically small at an average of 1.54 hectares. Areas of Field-Sectors are shown in Appendix A Table A1. Locations without any Field-Sectors with periods of low vegetation were subsequently removed from the analysis (see Section 2.3.3).

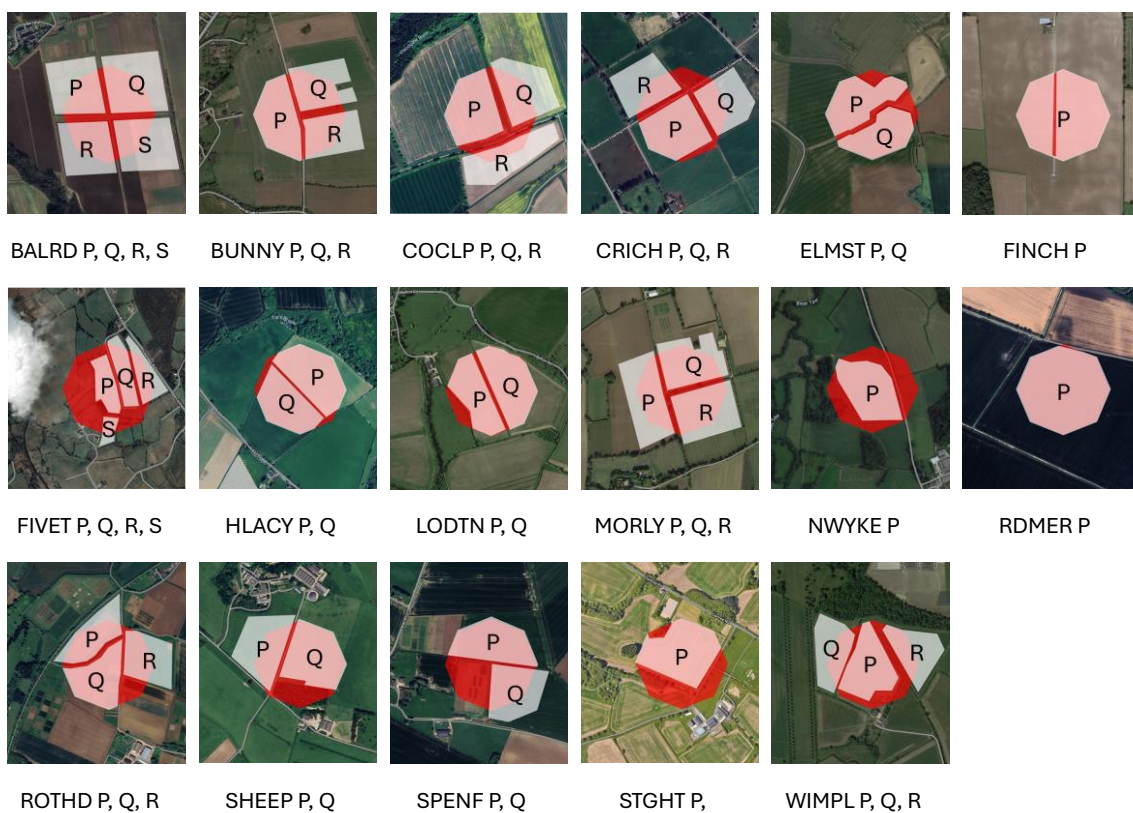


Figure 6. COSMOS-UK A&H Location_Field-Sector polygons: The red polygons approximate the COSMOS footprints, with the white polygons showing the delineated Field-Sectors used for backscattering averaging and vegetation assessment.

2.3.2. Field-Sector Average Backscattering and Vegetation Index

The average VV backscattering coefficient within the delineated Field-Sectors at each Location was calculated for all available S1 observations in the study period. Backscattering values were converted to linear form for averaging and then scaled back to dB. The NDVI pixel values were also averaged within the Field-Sectors for all cloud-free S2 images (Section 2.3.3).

2.3.3. Selection of Low-Vegetation Periods

As the vegetation canopy hinders the relationship between C-band SAR backscatter and SM, this analysis focused on times when the vegetation cover was low and the soil surface backscattering dominated the C-band response. Periods of low vegetation cover (L-periods) were selected for each study sector if they had NDVI values lower than 0.35 for a period encompassing at least 20 S1 observations. This threshold was chosen as being indicative of sparse to medium density herbaceous vegetation coverage, for which empirical and radiative transfer models demonstrate the dominance of C-band surface backscattering [26], whilst allowing sufficiently long periods for the analysis.

The L-periods were refined and verified visually by displaying NDVI maps for each site and S2 image using the GEE platform. The L-periods were sequentially labelled as L1, L2, L3, etc., for each Field-Sector, giving the naming convention of Location_Field-Sector_L-period. For example, BALRD_P_L2 denotes the COSMOS sensor Location “BALRD (Ballyruddery)”, Field-Sector “P” and the L-period (low vegetation period) number “2”. No L-periods were found for the FIVET Location (Field-Sectors P, Q, R, and S reviewed), whilst RDMER Location (Field P) L-periods did not overlap with COSMOS-UK SM data. This left a total of 15 analysis Locations, 30 Location_Field-Sectors, and 90 Location_Field-Sector_L-periods. These are shown in Figure 7.

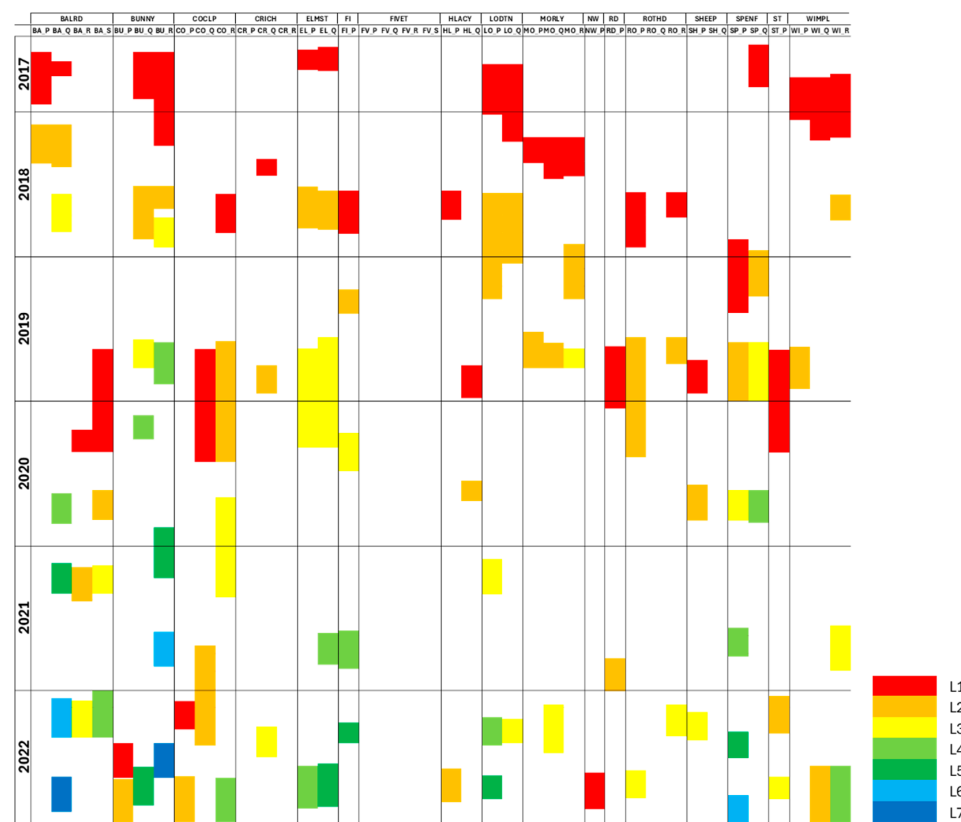


Figure 7. Illustration of the low vegetation periods (L—periods) per Location_Field—Sector.

2.3.4. S1 Time-Series Processing

Study Locations were imaged by S1 from different relative orbits with different SAR beam incidence angles. Despite the S1 data product used having been corrected for local incidence angle (through terrain correction), a shift between backscattering values corresponding to different orbits was observed for each Location. This shift was empirically estimated for each Location as follows: the average backscattering of each separate orbit's complete S1 time-series values (~8 years of data points, all covering the same complete time range) was calculated and compared to the average value for all orbits combined at that Location. The difference between both values, referred to as shift correction (SC), ranged between +1.396 and -1.567 and was applied as a single shift per orbit and Location, over S1 incidence angles ranging between 30.2° and 45.3°. This empirical correction allowed the integration of multi-orbit backscattering from each Location into a single, higher-frequency time series for subsequent analysis. Appendix B provides a detailed description of the SC, illustrating the effect of its application to the S1 data.

Subsequent to the SC, a smoother algorithm was applied to the S1 backscattering time series, as performed in [49]. The applied SC allowed the successful application of a rolling window average encompassing three consecutive observations, notably more conservative than others in the literature (e.g., 14 points in [49]) and therefore able to retain high-frequency moisture variation information.

2.3.5. Analysis of the Relationship Between VV Backscattering and Soil-Moisture

Scatter plots of the S1 VV backscattering coefficient (in dB), processed as described, versus SM were produced per Field-Sector for each study Location. The linear gradient observed in the scatter plots was measured and its goodness-of-fit assessed for each independent L-period (Location_Field-Sector_L-period). Mean values of the gradients within each Location were subsequently calculated. This was a more accurate measure than using

all L-period points for a Location due to the effect of soil roughness, which was considered largely stable during a single L-period but could change in between them. The S1 processing described in Section 2.3.4 improved the coefficient of determination (R^2) to the linear best-fit of S1 backscatter with SM by an average of 54%. The mean of the S1 vs. SM gradients was calculated for each Location.

3. Results and Discussion

Figure 8 depicts the results of the SM versus backscattering analysis for the UK-COSMOS Location COCLP. The Field-Sectors are shown in (a) as white polygons labelled P, Q, and R, overlaid on the COSMOS sensor footprint (in red). The SM versus S1 backscatter scatter plot of all the COCLP data (one L-period for COCLP_P, two L-periods for COCLP_Q, and three L-periods for COCLP_R) is shown in (b). Displays (c) to (f) are the scatter plots for each individual Location_Field-Sector_L-period with their linear regression annotated with their gradient and R^2 values. The S1 VV backscattering (in dB) and SM (in % VWC) display a clear linear trend. This display highlights the validity of each individual data series gradient (described by Location_Field-Sector_L-period), and the similarity of gradient between the different Location_Field-Sector_L-periods at a Location. This reinforces that a particular bare-soil S1 backscatter will be sensitive in a predictable way to SM.

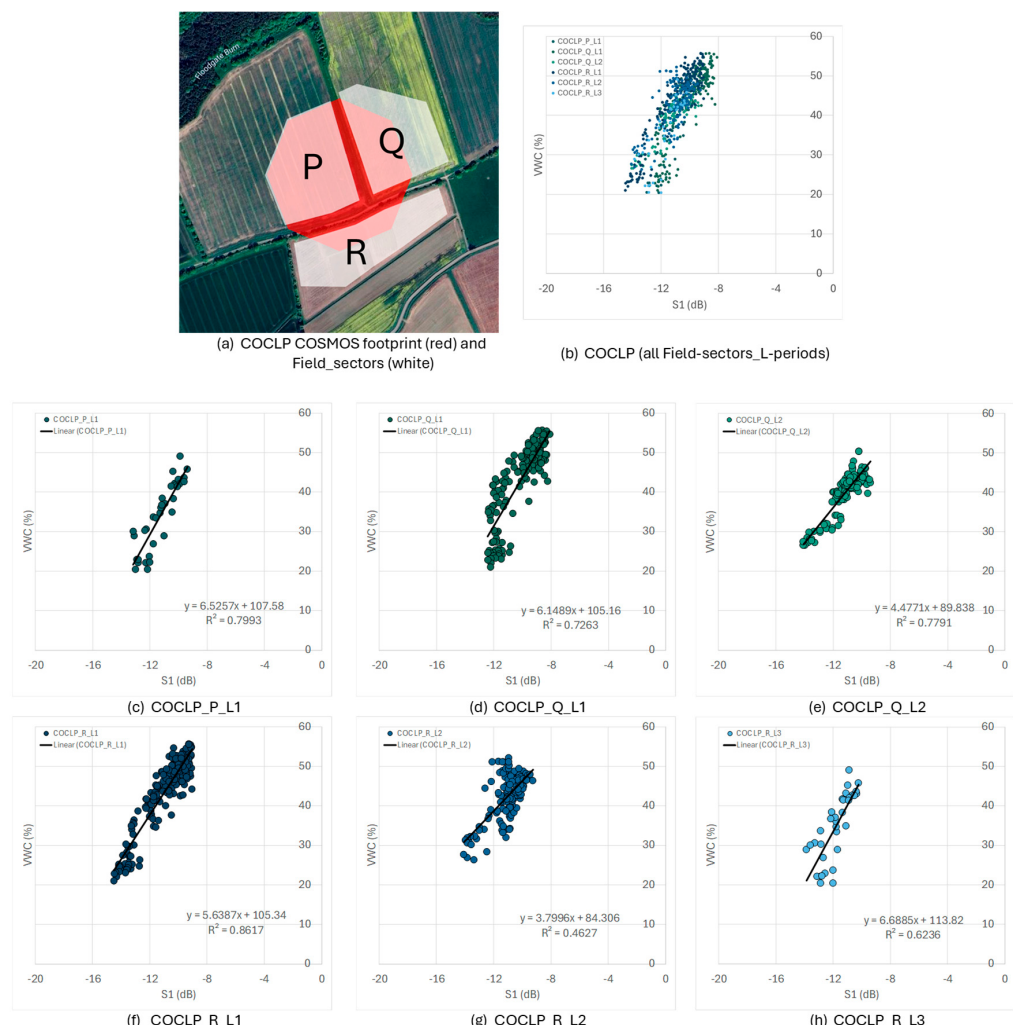


Figure 8. SM vs. S1 backscatter for the COCLP Location: (a) COSMOS footprint (red circle) and with COCLP Field–Sector (white polygons); (b) scatter plot of SM versus backscatter for all COCLP Sectors and L periods; (c–h) individual scatterplots for each Location_Field–Sector_L–period.

Figure 9 shows the SM versus S1 backscattering plots for all Field-Sector_L-periods by UK-COSMOS Location. The plots clearly show a linear relationship for the majority of Field-Sectors and bare-soil L-periods, as predicted by the semi-empirical linear equation [50].

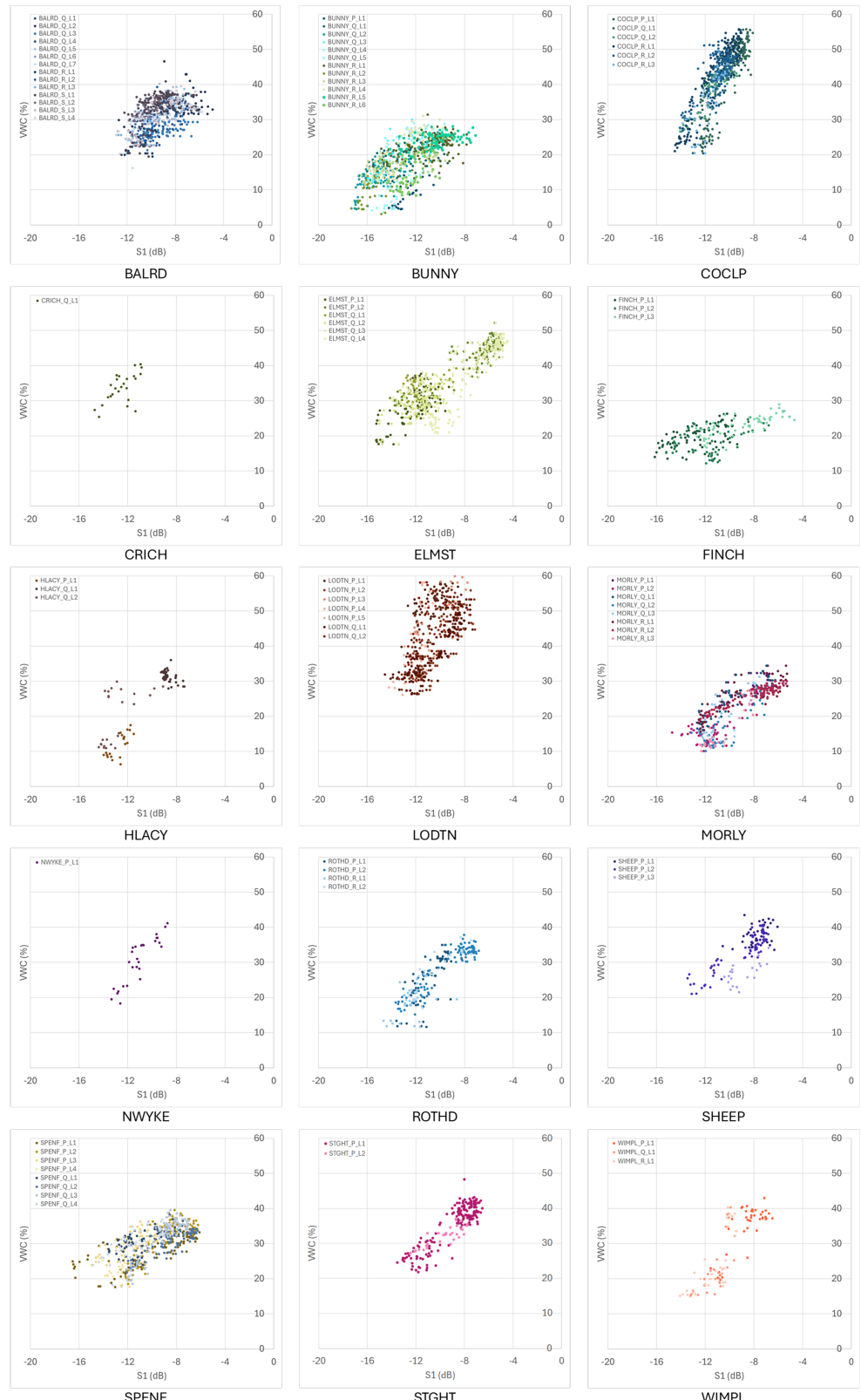


Figure 9. Scatter plots of SM (VWC in %) against S1 VV backscattering (dB) for all L–periods by UK-COSMOS Location.

Appendix C Table A4 details the mean gradients by Field-Sector and L-period for all Locations, along with other relevant information. Figure 10 shows the mean gradient by Location, arranged in order of increasing gradient (not related to soil texture at this point). The gradient was relatively invariant between L-periods at the same Location, highlighting the fact that it is a characteristic of each Location/Field-Sector. Mean gradients varied between FINCH with 0.70%/dB and COCLP at 5.52%/dB.

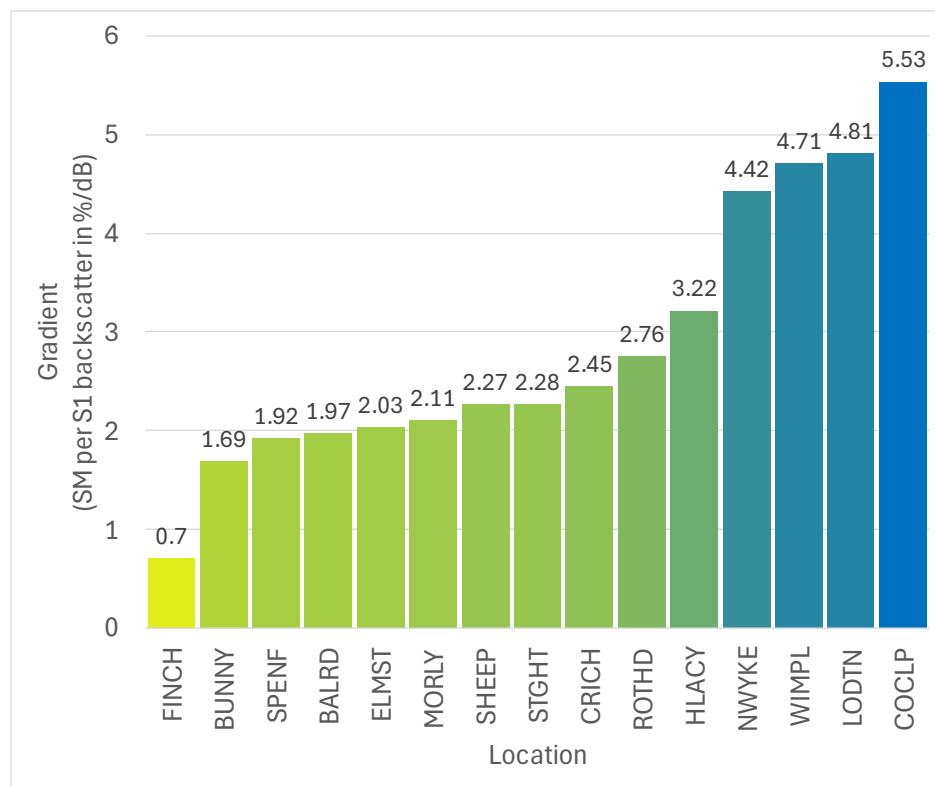


Figure 10. Mean SM versus backscattering gradient for all Field-Sector L-periods for each Location. Note: Locations are organized by gradient, not by soil characteristics. Figure 11 presents the gradients determined for each location as color-coded boxes on the soil texture triangle. The color-code indicates the gradient magnitude, while their location on the triangle is determined the UKSO soil texture description for the site.

The gradient distribution over the texture triangle suggests a pattern where Locations to the top (with higher clay content) have steeper gradients than those to the base of the soil triangle (lower clay content). The FINCH Location has the lowest gradient of all Locations; however, it is described as loam in UKSO. This low gradient may have been due to specific agricultural practices to improve drainage, or due to the presence of chalk (mentioned in the soil description) which also improves the drainage. However, this remains to be further investigated.

Figure 12 shows the 15 Locations, along with their soil texture description, in order of increasing (nominal, UKSO) clay content. This shows, similarly, that sandy and loamy Locations tend to have lower gradients whilst clayey Locations are on the opposite end: for example, the sandy BUNNY soil S1 response was more sensitive to SM, with a change of 1.69% SM per dB of S1 response, than the lower sensitivity of S1 response to SM of the clay LODTN soil with a change of 4.81% SM per dB of S1 response, a factor of 2.8. At the extremes of this study, sensitivity to SM varied between FINCH with a high sensitivity of 0.7% SM per dB of S1 response and COCLP with a low sensitivity of 5.53% SM per dB of S1 response, a factor of 7.9.

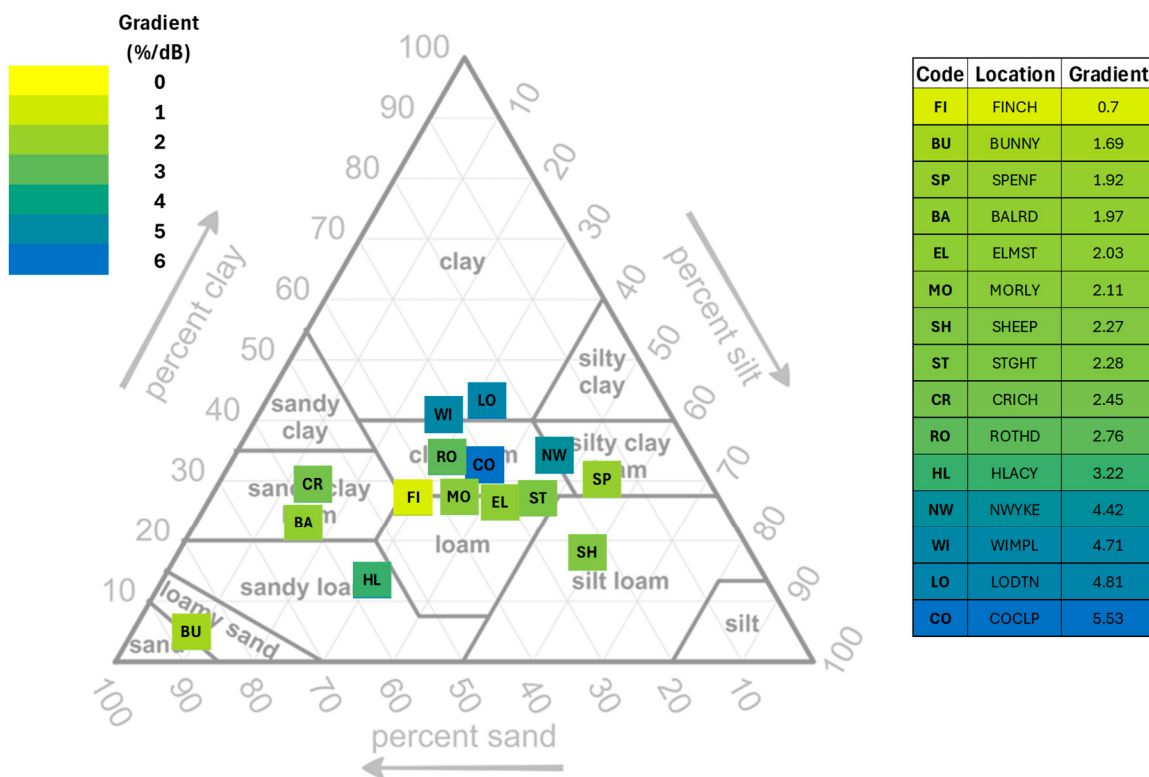


Figure 11. Mean SM versus backscattering gradient per Location, displayed on the soil texture triangle according to the Location's texture.

Soil Type COSMOS	Soil Type UKSO	Location	Mean %/dB
Loamy Sand/Sand	Sand/Sandy Loam	BUNNY	1.69
Loam	Sandy Loam	HLACY	3.22
Loam/Chalk	Silty Loam/Chalk	SHEEP	2.27
Sandy Loam	Clay loam/Sandy Loam	BALRD	1.97
Loam	Loam/Clay Loam/Chalk	FINCH	0.7
Clay Loam	Clay/Clayey Loam/Chalk	MORLY	2.11
Loam/Clay Loam	Loam/Clay Loam/Chalk	ELMST	2.03
Loam/Clay Loam	Loam/Clay Loam	STGHT	2.28
Loam	Clay Loam/Silty Loam	SPENF	1.92
Sandy Clay Loam	Clay loam/Sandy Loam	CRICH	2.45
Loam/Clay Loam	Clay Loam	COCLP	5.53
Clay Loam	Clay Loam	ROTHD	2.76
Loam/Clay Loam	Clay Loam/Silty Loam	NWYKE	4.42
Clay/Clay Loam	Clay/Clay Loam	WIMPL	4.71
Clay	Clay/Clayey Loam	LODTN	4.81

Figure 12. Location and soil texture in increasing gradient order. Gray highlighting shows Locations with chalk potentially associated.

It was also noted that four Locations (FINCH, ELMST, MORLY, and SHEEP) had chalk as part of their soil description: there is a possibility that chalk content may have increased the sensitivity of S1 backscatter to SM. This potential behavior is supported by [51] which suggests that calcium carbonate content improves the workability of soil, and that clay-sized chalk grains should be treated as silt.

4. Conclusions

This study found and quantified the impact of soil texture in the relationship between S1 VV backscattering and superficial SM. We analyzed this relationship using over

five years of SM data for crop fields and S1 VV backscattering, averaged over field sector. UK-COSMOS SM measurements were utilized as they are more representative of the field-wide moisture than readings from punctual probes. The semi-empirical linear relationship between SM and field-averaged S1 VV backscattering (dB) was observed in periods of low vegetation (L-periods), with coefficients of determination higher than 0.5 in 57% of the study sites. For a given location, the gradient of this relationship was maintained across L-periods although a shift may have occurred, presumably due to soil roughness changes (e.g., due to ploughing) in between L-periods.

Although limited by the number of sites that could be analyzed, our results strongly suggest that C-band VV backscattering is dependent on the soil texture with mean gradients varying between the high sensitivity of 1.69% VWC SM per dB of S1 response for a sandy soil and the low sensitivity of 4.81% VWC SM per dB of S1 response for a clay soil.

This finding is highly relevant as it lays the ground for a new approach to utilizing C-band SAR data, which is to retrieve soil texture properties at the crop-field scale. Given the increasing frequency and accuracy of gridded global precipitation and meteorological data and the availability of reliable soil-moisture simulation models, soil properties at the field scale can be optimized so that the simulated surface SM keeps a linear relationship with S1 VV backscattering field averages over low vegetation periods. This approach is supported by the results of [38], who successfully optimized soil parameters to align simulated soil-moisture trends with S1 VV backscattering time series.

Author Contributions: Conceptualization, C.A., I.S.-R., B.M.-C. and C.S.; methodology, C.S., B.M.-C. and I.S.-R.; data curation C.S.; investigation, C.S.; formal analysis, C.S.; visualization, C.S. and B.M.-C.; writing—original draft. C.S.; supervision, B.M.-C.; writing—review and editing, C.A. and B.M.-C. All authors have read and agreed to the published version of the manuscript.

Funding: This work was initially supported by the SPace Research & Innovation Network for Technology (SPRINT) Programme, with funding from UK Research and Innovation and by Mantle-Labs Ltd. The University of Surrey is funding a PhD research that expands the former project.

Data Availability Statement: The COSMOS original data presented in the study are openly available from the Environmental Information Data Centre at <https://eidc.ac.uk> (accessed on 1 December 2022). The Sentinel data presented in the study are openly available from the ESA Copernicus Open Access hub at <https://scihub.copernicus.eu> (accessed on 1 December 2022). The UKSO data presented in the study are openly available from the UK Soil Observatory at <https://www.ukso.org/> (accessed on 1 February 2024).

Acknowledgments: The authors would like to thank the UK Centre for Ecology & Hydrology for providing the UK COSMOS VWC experimental data used in this study. We also express our sincere gratitude to Professor David Robinson for his insightful suggestions.

Conflicts of Interest: The author Clement Atzberger is employed by the Mantle-Labs Ltd. The funders had no role in the design of the study; in the collection, analyses, or interpretation of data; in the writing of the manuscript; or in the decision to publish the results.

Appendix A. List of Fields and Their Surface Area

Table A1. Location_Field-Sector areas.

Location_Field-Sector	Area (ha)
BALRD_P	4.27
BALRD_Q	5.26
BALRD_R	4.12
BALRD_S	4.58
BUNNY_P	5.12

Table A1. *Cont.*

Location_Field-Sector	Area (ha)
BUNNY_Q	4.57
BUNNY_R	4.21
COCLP_P	5.02
COCLP_Q	4.90
COCLP_R	4.59
CRICH_P	4.85
CRICH_Q	4.06
CRICH_R	4.25
ELMST_P	5.11
ELMST_Q	4.41
FINCH_P	11.09
FIVET_P	1.79
FIVET_Q	1.86
FIVET_R	1.90
FIVET_S	0.62
HLACY_P	5.67
HLACY_Q	4.79
LODTN_P	4.32
LODTN_Q	5.41
MORLY_P	5.97
MORLY_Q	5.09
MORLY_R	5.60
NWYKE_P	5.75
RDMER_0	11.52
ROTHD_P	4.05
ROTHD_Q	4.52
ROTHD_R	4.30
SHEEP_P	5.70
SHEEP_Q	6.21
SPENF_P	5.11
SPENF_Q	4.68
STGHT_P	6.73
WIMPL_P	4.99
WIMPL_Q	4.14
WIMPL_R	4.03

Appendix B. Empirical Shift Correction

Most Locations in this study were imaged from four S1 orbits. For example, the STGHT S1 backscatter time-series consisted of interleaved, roughly daily observations from orbits numbered 30, 81, 132, and 154, of which orbits 30 and 132 were ascending and 81 and 154 were descending. Figure A1 shows the STGHT_P Location along with its all-orbits S1 backscatter time-series.

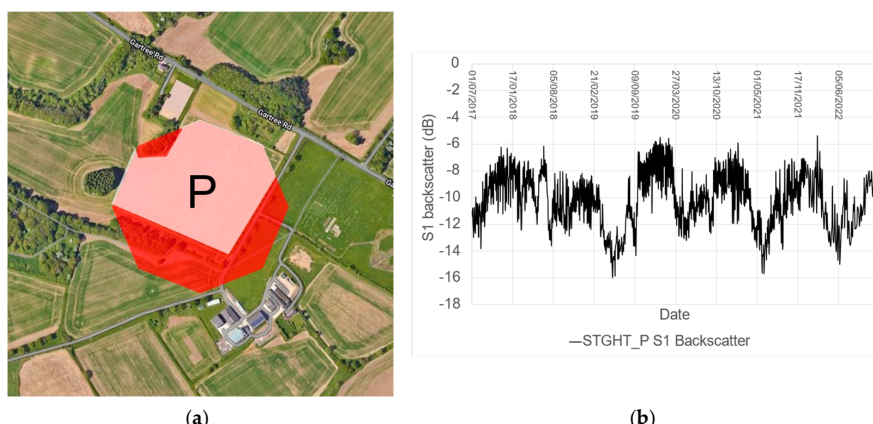


Figure A1. (a) STGHT_P Location and (b) recorded S1 backscatter 01/07/2017 to 30/11/2022.

C-band backscattering was dependent on the observation geometry, having a non-linear reduction with increased incidence angle. Given the relatively small size of the Locations, the change of S1 incidence angle across them was very low, and a single SC was appropriate per orbit and Location. Table A2 illustrates the range of incidence angles for STGHT.

Table A2. STGHT orbit information.

STGHT Orbit	Ascending/ Descending	Average Angle (Degrees)	Minimum Angle (Degrees)	Maximum Angle (Degrees)
30	Ascending	44.51	44.45	44.57
81	Descending	42.05	41.85	42.08
132	Ascending	36.62	36.54	36.70
154	Descending	33.69	33.66	33.73

Figure A2 displays a reduced date range for the recorded S1 backscatter in black, along with the recorded angle for each observation, showing a systematic relationship between the incidence angle and the value of the S1 backscatter.

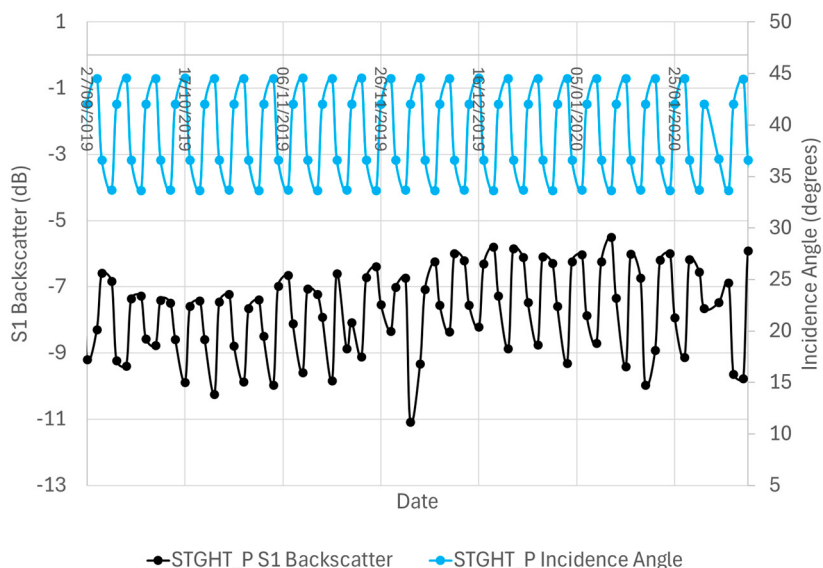
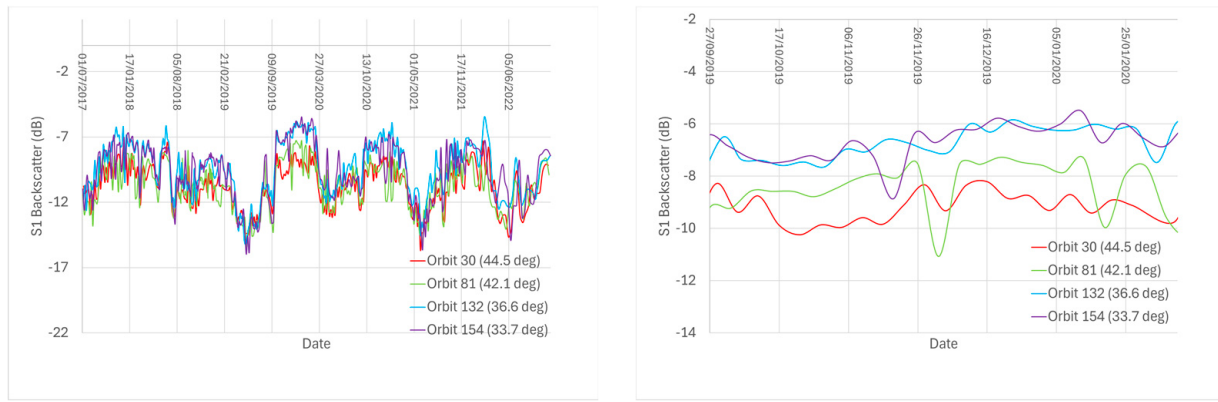


Figure A2. STGHT Location S1 backscatter for all orbits (black) and incidence angle (blue) for 27/09/2019 to 09/02/2020.

The S1 time-series for all observations (i.e., including both high and low vegetation periods) was separated into its four component orbits (with a corresponding four times reduction in observation frequency per time series). These are shown in Figure A3. This shows the difference, for this single Location, between the average S1 backscatter value per orbit: e.g., the red orbit 30, at 44.5 degrees, was consistently around 1.5 dB lower than the purple orbit 154 at 33.7 degrees.

As the requirement for the study was to calculate gradients of S1 backscatter against SM per Location (rather than relatively between Locations), a single correction was applied to each orbit per Location in order to align the mean backscatter over the entire time-series. This is shown in Table A3 where each orbit's mean S1 value (e.g., -10.77 dB, -9.67 dB) is compared to the mean of the entire S1 time series (-10.14).



(a) Separated orbits 01/07/2017 to 30/11/2022

(b) Separated orbits 27/09/2019 to 09/02/2020

Figure A3. STGHT Location S1 backscatter separated into individual orbits.**Table A3.** STGHT shift corrections.

STGHT Orbit	Average Angle (Degrees)	Average S1 per Orbit (dB)	Average of All S1 (dB)	Correction Applied (dB)
30	44.51	-10.77	-10.14	0.63
81	42.05	-10.7	-10.14	0.56
132	36.62	-9.42	-10.14	-0.72
154	33.69	-9.67	-10.14	-0.47

Figure A4 shows these corrections graphically.

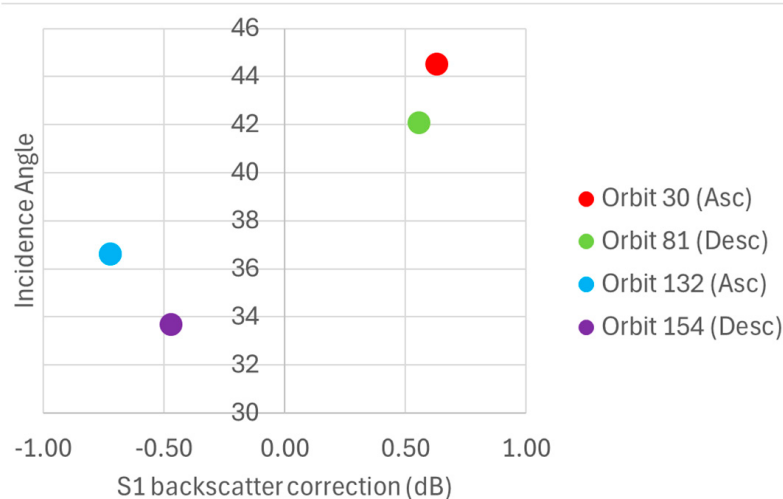
**Figure A4.** Orbit– and Location–based single value corrections applied to STGHT location.

Figure A5 shows the S1 backscatter for this STGHT Location, separated into orbits, without and with the correction. This clearly displays the effect of the correction, reducing the systematic shift between the different orbits.

To ensure that this correction which aligned the mean S1 values of the individual orbits (a) improved the reliability of the data and (b) did not skew subsequent analysis, the S1 backscatter vs. SM scatterplots were checked. An example for the STGHT_P_L1 period is shown in Figure A6: the empirical correction shifted the individual orbit points in the x -axis but did not change the gradient or R^2 values.

Figure A7 shows STGHT_P_L1, color-coded by orbit, without and with the application of the calculated shift corrections. It can be seen that the linear regressions for each orbit now

aligned, whilst retaining their individual gradients. This application of a single correction per orbit per Location therefore corrected any remaining variation in S1 backscatter.

This analysis and correction generation was performed within every Location, using the entire time-series available. These are shown in Figure A8.

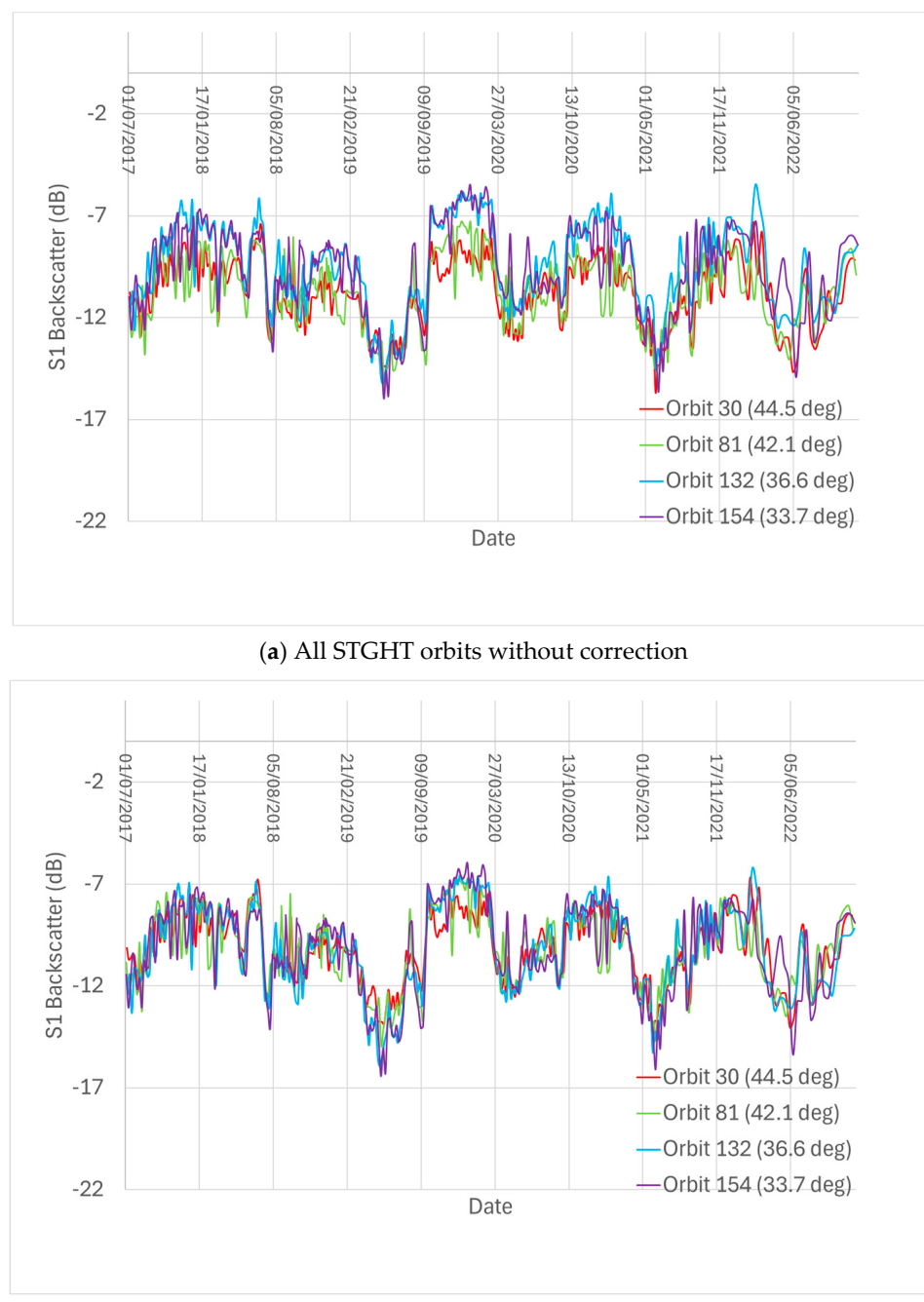


Figure A5. S1 backscatter for each orbit of the STGHT Location: **(a)** raw and **(b)** with the application of the calculated shift correction.

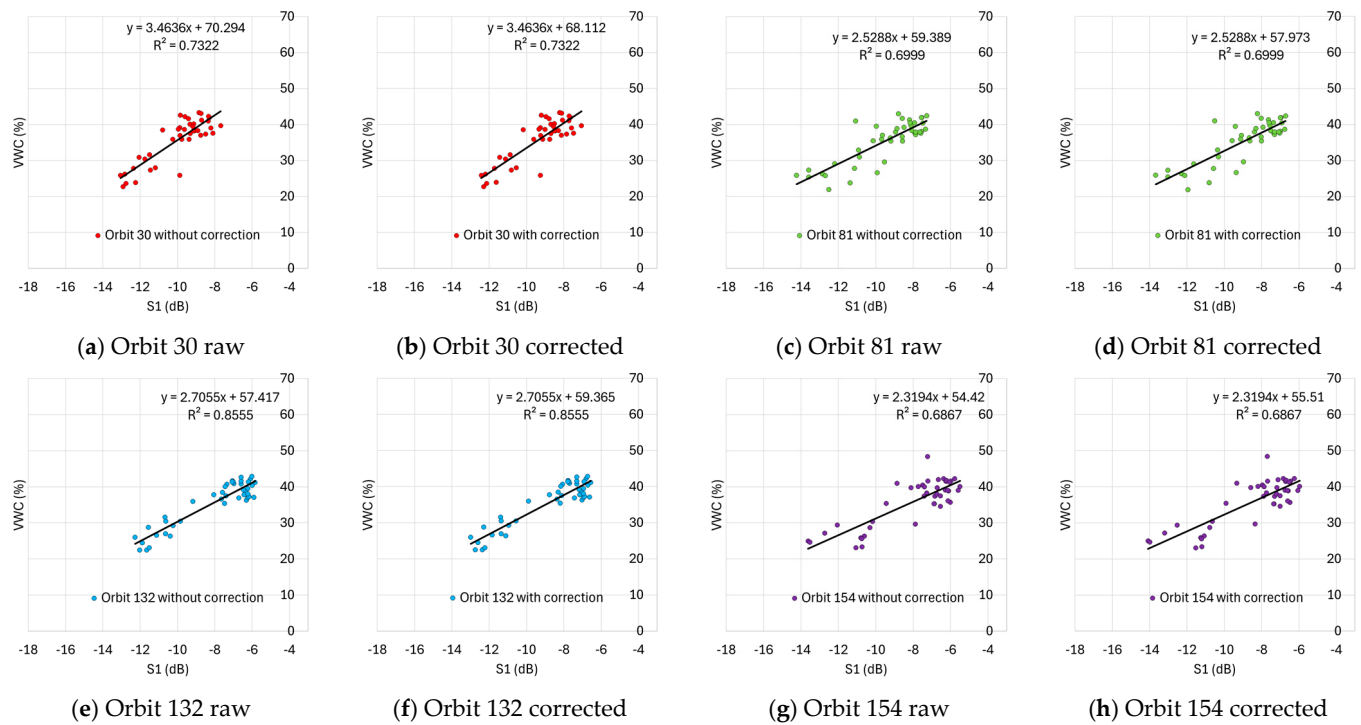


Figure A6. Each orbit of the STGHT location L—period 1, as recorded (a,c,e,g), and with the correction (b,d,f,h).

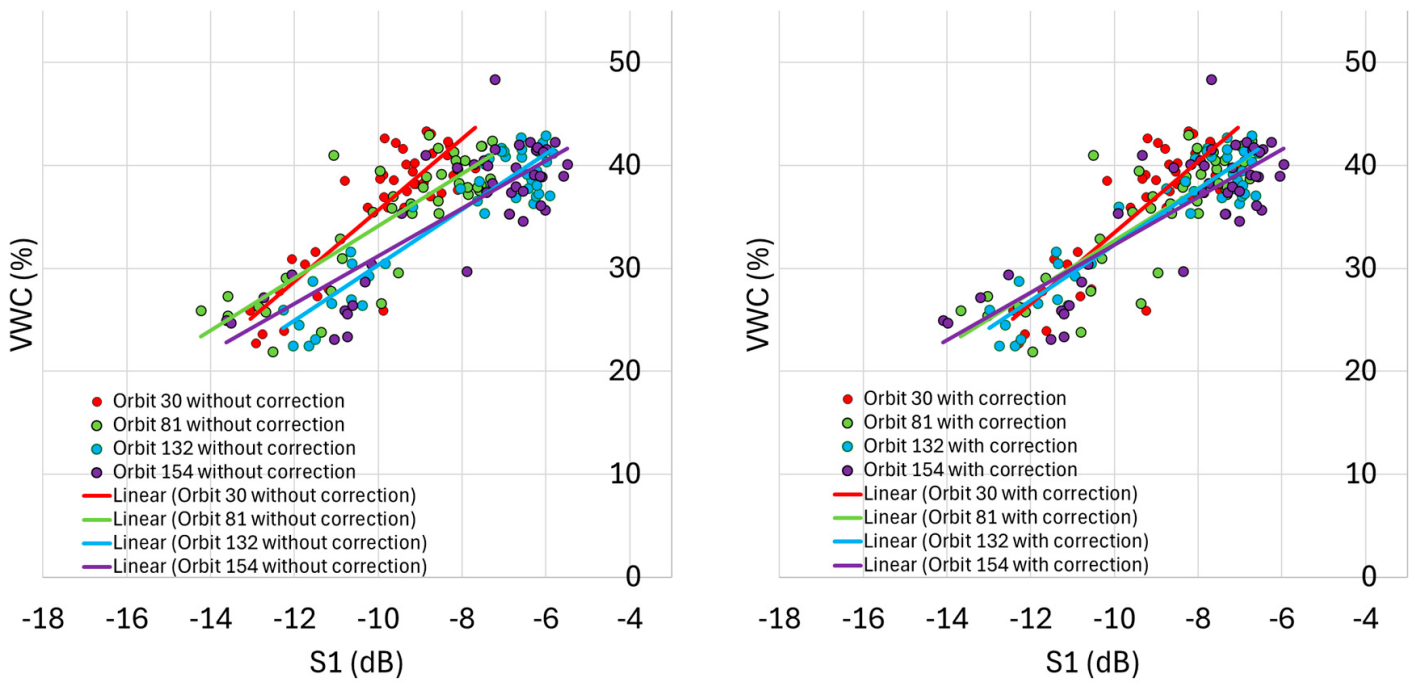


Figure A7. All orbits for the STGHT location, with linear regressions: (a) raw and (b) with shift correction.

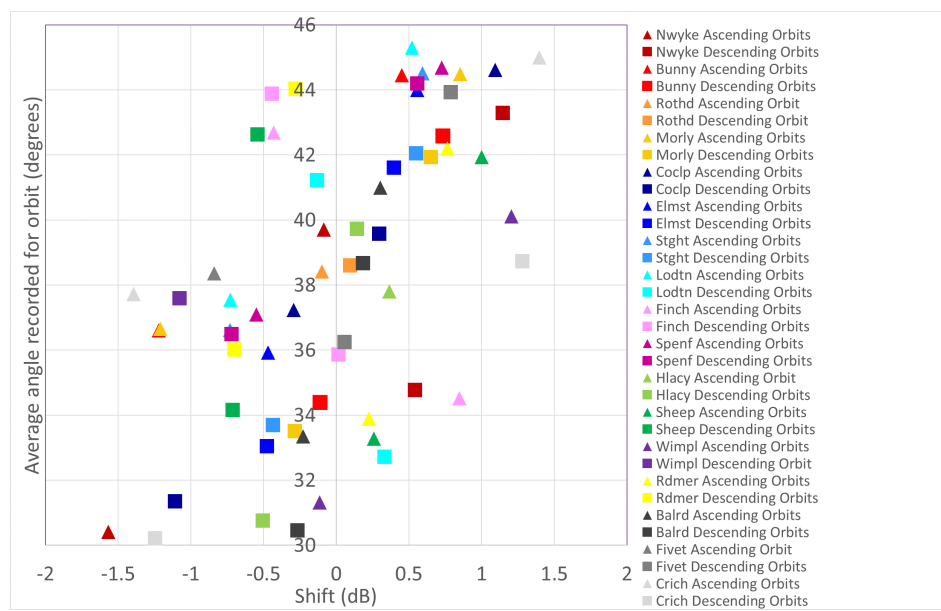


Figure A8. Empirical shift correction values with angle.

Appendix C. Information per Location_Field-Sector_L-Period

Table A4. Gradients, number of points, and R^2 per Location_Field-Sector_L-period.

Location	Mean Gradient (Location)	No. of Gradients (Location)	Location_Field	Mean Gradient (Field)	No. of Gradients (Field)	L-Period	Start Date	End Date	No. of Coincident Points	Gradient	R^2
BALRD	1.97	14	BALRD_Q	1.59	7	L1	26/08/2017	02/10/2017	24	1.71	0.597
						L2	02/02/2018	18/05/2018	63	0.94	0.245
						L3	27/07/2018	30/10/2018	92	0.83	0.286
						L4	22/08/2020	05/11/2020	50	1.14	0.279
						L5	16/02/2021	02/05/2021	48	2.86	0.717
						L6	22/01/2022	29/04/2022	32	1.09	0.323
						L7	07/08/2022	03/11/2022	28	2.54	0.505
			BALRD_R	2.48	3	L1	13/03/2020	07/05/2020	36	3.36	0.833
						L2	26/02/2021	22/05/2021	58	2.54	0.375
						L3	27/01/2022	29/04/2022	30	1.56	0.430
			BALRD_S	2.27	4	L1	23/08/2019	07/05/2020	168	2.21	0.345
						L2	12/08/2020	26/10/2020	50	2.70	0.455
						L3	21/02/2021	02/05/2021	46	2.97	0.736
						L4	02/01/2022	29/04/2022	38	1.21	0.416
BUNNY	1.69	12	BUNNY_P	1.58	1	L1	14/05/2022	09/08/2022	30	1.58	0.174
			BUNNY_Q	1.82	5	L1	03/08/2017	28/11/2017	77	0.96	0.332
						L2	30/07/2018	18/11/2018	111	1.77	0.417
						L3	29/07/2019	09/10/2019	47	2.28	0.615
						L4	06/02/2020	06/04/2020	41	1.66	0.610
						L5	13/07/2022	18/10/2022	32	2.45	0.502
			BUNNY_R	1.59	6	L1	03/08/2017	26/03/2018	156	1.02	0.307
						L2	26/07/2018	02/09/2018	37	3.14	0.443
						L3	24/09/2018	08/12/2018	74	1.11	0.376
						L4	05/08/2019	18/11/2019	68	2.32	0.550
						L5	15/11/2020	25/03/2021	83	0.67	0.275
						L6	08/08/2021	01/11/2021	56	1.28	0.136
COCLP	5.53	6	COCLP_P	6.53	1	L1	05/08/2022	28/11/2022	36	6.53	0.799
			COCLP_Q	5.31	2	L1	23/08/2019	01/06/2020	185	6.15	0.726
			COCLP_R	5.34	3	L2	11/09/2021	19/05/2022	117	4.48	0.779
						L1	03/08/2019	01/06/2020	198	5.64	0.862
CRICH	2.45	1	CRICH_Q	2.45		L2	29/09/2020	12/05/2021	165	3.69	0.289
			L3	10/08/2022		28/11/2022	35	6.69	0.624		
ELMST	2.03	6	ELMST_P	2.27	2	L1	08/07/2018	21/10/2018	106	2.32	0.516
			ELMST_Q	1.91	4	L2	22/08/2019	26/04/2020	162	2.21	0.841
						L1	21/07/2017	19/09/2017	40	0.86	0.173
						L2	18/07/2018	24/10/2018	103	2.00	0.424
						L3	23/07/2019	26/04/2020	181	2.10	0.824
						L4	11/08/2021	28/10/2021	52	2.69	0.210

Table A4. Cont.

Location	Mean Gradient (Location)	No. of Gradients (Location)	Location_Field	Mean Gradient (Field)	No. of Gradients (Field)	L-Period	Start Date	End Date	No. of Coincident Points	Gradient	R ²			
FINCH	0.70	3	FINCH_P	0.70	3	L1	25/03/2019	24/05/2019	38	0.66	0.203			
						L2	22/03/2020	25/06/2020	63	0.57	0.128			
						L3	04/08/2021	07/11/2021	62	0.88	0.557			
HLACY	3.22	2	HLACY_P	3.49	1	L1	18/07/2022	08/10/2022	20	3.49	0.583			
			HLACY_Q	2.95	1	L1	02/10/2019	23/12/2019	40	-1.76	0.266			
			LODTN_P	4.40	5	L2	20/07/2020	08/09/2020	25	2.95	0.317			
LODTN	4.81	7				L1	02/09/2017	07/01/2018	85	2.29	0.151			
						L2	24/07/2018	17/04/2019	219	4.18	0.655			
						L3	05/02/2021	04/05/2021	35	4.76	0.581			
						L4	10/03/2022	19/05/2022	20	9.09	0.709			
						L5	04/08/2022	01/10/2022	19	2.45	0.532			
						L1	24/07/2018	17/01/2019	165	3.65	0.716			
						L2	10/03/2022	10/05/2022	20	7.22	0.535			
MORLY	2.11	8	MORLY_P	1.72	2	L1	05/03/2018	09/05/2018	44	1.76	0.606			
			L2	11/07/2019	09/10/2019	58	1.69	0.439						
			L1	05/03/2018	18/06/2018	68	1.96	0.737						
			L2	07/08/2019	09/10/2019	41	2.36	0.640						
			L3	07/02/2022	07/06/2022	40	2.70	0.650						
			L1	05/03/2018	11/06/2018	64	1.67	0.750						
			L2	30/11/2018	17/04/2019	99	1.35	0.872						
			L3	22/08/2019	09/10/2019	31	3.40	0.831						
NWYKE	4.42	1	NWYKE_P	4.42	1	L1	28/07/2022	26/10/2022	28	4.42	0.793			
ROTHD	2.76	4	ROTHD_P	3.34	2	L1	23/07/2018	08/12/2018	68	3.91	0.588			
			ROTHD_R	2.19	2	L2	23/07/2019	21/05/2020	100	2.76	0.849			
			L1	23/07/2018	24/09/2018	30	1.90	0.252						
SHEEP	2.27	3	SHEEP_P	2.27	3	L2	02/02/2022	17/06/2022	22	2.48	0.881			
			L1	19/09/2019		11/12/2019	57	1.42	0.239					
			L2	30/07/2020		28/10/2020	59	3.61	0.405					
SPENF	1.92	8	SPENF_P	1.91	4	L3	25/02/2022	06/05/2022	22	1.79	0.425			
						L1	18/11/2018	22/05/2019	126	1.21	0.626			
						L2	05/08/2019	31/12/2019	97	2.76	0.705			
						L3	12/08/2020	28/10/2020	51	1.84	0.320			
						L4	28/07/2021	08/10/2021	47	1.82	0.376			
			SPENF_Q	1.94	4	L1	14/07/2017	29/10/2017	71	1.21	0.401			
						L2	16/12/2018	10/04/2019	74	1.53	0.621			
						L3	05/08/2019	31/12/2019	97	3.12	0.740			
						L4	12/08/2020	02/11/2020	55	1.90	0.533			
STGHT	2.28	2	STGHT_P	2.28	2	L1	25/08/2019	09/05/2020	170	2.90	0.787			
			L2	16/01/2022	19/04/2022	31	1.66	0.683						
WIMPL	4.71	3	WIMPL_P	3.92	1	L1	17/08/2019	30/11/2019	40	3.92	0.623			
			WIMPL_Q	5.77	1	L1	10/07/2022	30/11/2022	31	5.77	0.575			
			WIMPL_R	4.43	1	L1	10/07/2022	25/11/2022	31	4.43	0.562			

References

1. The Global Climate Observing System, “Essential Climate Variables”. 2023. Available online: <https://gcos.wmo.int/en/essential-climate-variables/> (accessed on 1 September 2023).
2. Jadidoleslam, N.; Mantilla, R.; Krajewski, W.; Goska, R. Investigating the role of antecedent SMAP satellite soil moisture, radar rainfall and MODIS vegetation on runoff production in an agricultural region. *J. Hydrol.* **2019**, *579*, 124210. [CrossRef]
3. Sanz-Ramos, M.; Martí-Cardona, B.; Bladé, E.; Seco, I.; Amengual, A.; Roux, H.; Romero, R. NRCS-CN estimation from onsite and remote sensing data for management of a reservoir in the Eastern Pyrenees. *J. Hydrol. Eng.* **2020**, *25*, 05020022. [CrossRef]
4. Rossato, L.; Alvalá, R.; Marengo, J.; Zeri, M.; Cunha, A.; Pires, L.; Barbosa, H. Impact of Soil Moisture on Crop Yields over Brazilian Semi-arid. *Front. Environ. Sci.* **2017**, *5*, 73. [CrossRef]
5. Brocca, L.; Tarpanelli, A.; Filippucci, P.; Dorigo, W.; Zaussinger, F.; Gruber, A.; Fernández-Prieto, D. How much water is used for irrigation? A new approach exploiting coarse resolution satellite soil moisture products. *Int. J. Appl. Earth Obs. Geoinf.* **2018**, *73*, 752–766. [CrossRef]
6. Liu, Y.; Qian, J.; Yue, H. Combined Sentinel-1A with Sentinel-2A to Estimate Soil Moisture in Farmland. *IEEE J. Sel. Top. Appl. Earth Obs. Remote Sens.* **2020**, *14*, 1292–1310. [CrossRef]
7. Seneviratne, S.; Corti, T.; Davin, E.; Hirschi, M.; Jaeger, E.; Lehner, I.; Orlowsky, B.; Teuling, A. Investigating soil moisture-climate interactions in changing climate: A review. *Earth Sci. Rev.* **2010**, *99*, 125–161. [CrossRef]
8. Tao, F.; Yokozawa, M.; Hayashi, Y.; Lin, E. Future Climate Change, the Agricultural Water Cycle, and Agricultural Production in China. *Agric. Ecosyst. Environ.* **2003**, *95*, 203–215. [CrossRef]
9. Green, J.; Seneviratne, S.; Berg, A.; Findell, K.; Hagemann, S.; Lawrence, D.; Gentine, P. Large influence of soil moisture on long-term terrestrial carbon uptake. *Nature* **2019**, *565*, 476–479. [CrossRef] [PubMed]
10. Ulaby, F.; Batlivala, P.; Dobson, M. Microwave Backscatter Dependence on Surface Roughness, Soil Moisture, and Soil Texture: Part I-Bare Soil. *IEEE Trans. Geosci. Electron.* **1978**, *16*, 286–295. [CrossRef]

11. Kerr, Y.H.; Waldteufel, P.; Wigneron, J.P.; Delwart, S.; Cabot, F.; Boutin, J.; Escorihuela, M.J.; Font, J.; Reul, N.; Gruhier, C.; et al. The SMOS Mission: New Tool for Monitoring Key Elements of the Global Water Cycle. *Proc. IEEE* **2010**, *98*, 666–687. [[CrossRef](#)]
12. Entekhabi, D.; Njoku, E.G.; O'Neill, P.E.; Kellogg, K.H.; Crow, W.T.; Edelstein, W.N.; Entin, J.K.; Goodman, S.D.; Jackson, T.J.; Johnson, J.; et al. The Soil Moisture Active Passive (SMAP) Mission. *Proc. IEEE* **2010**, *98*, 704–716. [[CrossRef](#)]
13. National Snow and Ice Data Center. AMSR-E/Aqua Daily L3 Surface Soil Moisture, Interpretive Parameters, & QC EASE-Grids, Version 2. 2023. Available online: https://nsidc.org/data/ae_land3/versions/2 (accessed on 1 September 2023).
14. Kerr, Y.H.; Waldteufel, P.; Richaume, P.; Wigneron, J.P.; Ferrazzoli, P.; Mahmoodi, A.; Al Bitar, A.; Cabot, F.; Gruhier, C.; Juglea, S.E.; et al. The SMOS soil moisture retrieval algorithm. *IEEE Trans. Geosci. Remote Sens.* **2012**, *50*, 1384–1403. [[CrossRef](#)]
15. EUMETSAT. ASCAT. 2023. Available online: <https://www.eumetsat.int/ascat> (accessed on 1 September 2023).
16. Copernicus Global Land Service. Surface Soil Moisture. 2023. Available online: <https://land.copernicus.eu/global/products/ssm> (accessed on 1 September 2023).
17. NASA. SMAP Soil Moisture Active Passive Data Products. 2023. Available online: <https://smap.jpl.nasa.gov/data/> (accessed on 1 September 2023).
18. Beale, J.; Waine, T.; Evans, J.; Corstanje, R. A Method to Assess the Performance of SAR-Derived Surface Soil Moisture Products. *IEEE J. Sel. Top. Appl. Earth Obs. Remote Sens.* **2021**, *14*, 4504–4516. [[CrossRef](#)]
19. European Space Agency. Sentinel-1. Available online: <https://sentinels.copernicus.eu/web/sentinel/copernicus/sentinel-1> (accessed on 30 January 2025).
20. Li, Z.; Leng, P.; Zhou, C.; Chen, K.; Zhou, F.; Shang, G. Soil Moisture Retrieval from Remote Sensing Measurements: Current Knowledge and Directions for the Future. *Earth-Sci. Rev.* **2021**, *218*, 103673. [[CrossRef](#)]
21. Petropoulos, G.P.; Ireland, G.; Srivastava, P.; Ioannou-Katidis, P. An Appraisal of the Accuracy of Operational Soil Moisture Estimates from SMOS MIRAS Using Validated In Situ Observations Acquired in a Mediterranean Environment. *Int. J. Remote Sens.* **2014**, *35*, 5239–5250. [[CrossRef](#)]
22. Yin, J.; Zhan, X.; Liu, J.; Moradkhani, H.; Fang, L.; Walker, J. Near-real-time one-kilometre Soil Moisture Active Passive soil moisture data product. *Hydrol. Process.* **2020**, *34*, 4083–4096. [[CrossRef](#)]
23. Bauer-Marschallinger, B.; Freeman, V.; Cao, S.; Paulik, C.; Schaufler, S.; Stachl, T.; Modanesi, S.; Massari, C.; Ciabatta, L.; Brocca, L.; et al. Toward Global Soil Moisture Monitoring with Sentinel-1: Harnessing Assets and Overcoming Obstacles. *IEEE Trans. Geosci. Remote Sens.* **2019**, *57*, 520–539. [[CrossRef](#)]
24. Balenzano, A.; Mattia, F.; Satalino, G.; Lovergne, F.P.; Palmisano, D.; Peng, J.; Marzahn, P.; Wegmüller, U.; Cartus, O.; Dąbrowska-Zielińska, K.; et al. Sentinel-1 soil moisture at 1 km resolution: A validation study. *Remote Sens. Environ.* **2021**, *263*, 112554. [[CrossRef](#)]
25. Verhoest, N.; Lievens, H.; Wagner, W.; Alvarez-Mozos, J.; Moran, M.; Mattia, F. On the Soil Roughness Parameterization Problem in Soil Moisture Retrieval of Bare Surfaces from Synthetic Aperture Radar. *Sensors* **2008**, *8*, 4213–4248. [[CrossRef](#)]
26. Bindlish, R.; Barros, A. Parameterization of vegetation backscatter in radar-based, soil moisture estimation. *Remote Sens. Environ.* **2001**, *76*, 130–137. [[CrossRef](#)]
27. Ulaby, F.; Long, D. *Microwave Radar and Radiometric Remote Sensing*; Artech House: Norwood, MA, USA, 2015.
28. Hou, A.Y.; Kakar, R.K.; Neeck, S.; Azbarzin, A.A.; Kummerow, C.D.; Kojima, M.; Oki, R.; Nakamura, K.; Iguchi, T. The global precipitation measurement mission. *Bull. Am. Meteorol. Soc.* **2014**, *95*, 701–722. [[CrossRef](#)]
29. NASA. IMERG: Integrated Multi-Satellite Retrievals for GPM. Available online: <https://gpm.nasa.gov/data/imerg> (accessed on 1 September 2023).
30. Huffman, G.; Bolvin, D. *Version 1.2 GPCP One-Degree Daily Precipitation Data Set Documentation*; NASA Goddard Space Flight Center: Greenbelt, MD, USA, 2013.
31. Xie, P.; Chen, M.; Shi, W. CPC unified gauge-based analysis of global daily precipitation. In Proceedings of the 24th Conference on Hydrology, Atlanta, GA, USA, 18–21 January 2010.
32. Huffman, G.J.; Bolvin, D.T.; Nelkin, E.J.; Wolff, D.B.; Adler, R.F.; Gu, G.; Hong, Y.; Bowman, K.P.; Stocker, E.F. The TRMM Multisatellite Precipitation Analysis (TMPA): Quasi-Global, Multiyear, Combined-Sensor Precipitation Estimates at Fine Scales. *J. Hydrometeorol.* **2007**, *8*, 38–55. [[CrossRef](#)]
33. Ushio, T.; Sasashige, K.; Kubota, T.; Shige, S.; Okamoto, K.; Aonashi, K.; Kawasaki, Z. A Kalman Filter Approach to the Global Satellite Mapping of Precipitation (GSMP) from Combined Passive Microwave and Infrared Radiometric Data. *J. Meteorol. Soc. Japan. Ser. II* **2009**, *87 Pt A*, 137–151. [[CrossRef](#)]
34. Sorooshian, S.; Hsu, K.-L.; Gao, X.; Gupta, H.V.; Imam, B.; Braithwaite, D. Evaluation of PERSIANN system satellite-based estimates of tropical rainfall. *Bull. Am. Meteorol. Soc.* **2000**, *81*, 2035–2046. [[CrossRef](#)]
35. National Centers for Environmental Information. National Oceanic and Atmospheric Administration, Precipitation—CMORPH CDR. Available online: <https://www.ncei.noaa.gov/products/climate-data-records/precipitation-cmorph> (accessed on 1 September 2023).

36. GloH20. MSWEP Multi-Source Weighted-Ensemble Precipitation. Available online: <https://www.gloh2o.org/mswep/> (accessed on 1 September 2023).
37. Climate Hazards Center UC Santa Barbara. CHIRPS: Rainfall Estimates from Rain Gauge and Satellite Observations. Available online: <https://www.chc.ucsb.edu/data/chirps> (accessed on 1 September 2023).
38. Martí-Cardona; Seco, I.; Atzberger, C. *Sentinel-1 Time Series and Hydrological Modelling to Retrieve Soil Moisture at the Field Scale*; CLiving Planet Symposium: Bonn, Germany, 2022.
39. UK Centre for Ecology and Hydrology. Cosmic-Ray Soil Moisture Monitoring Network. 2023. Available online: <https://cosmos.ceh.ac.uk/> (accessed on 1 September 2023).
40. Department for Environment Food and Rural Affairs. LIDAR Composite Digital Terrain Model (DTM)—1m. 2022. Available online: <https://environment.data.gov.uk/dataset/13787b9a-26a4-4775-8523-806d13af58fc> (accessed on 1 September 2023).
41. Zreda, M.S.W.; Zeng, X.; Zweck, C.; Desilets, D.; Franz, T.; Rosolem, R. COSMOS: The COsmic-ray Soil Moisture Observing System. *Hydrol. Earth Syst. Sci.* **2012**, *16*, 4079–4099. [[CrossRef](#)]
42. Robinson, D.A.; Campbell, C.S.; Hopmans, J.W.; Hornbuckle, B.K.; Jones, S.B.; Knight, R.; Ogden, F.; Selker, J.; Wendoroth, O. Soil Moisture Measurement for Ecological and Hydrological Watershed-Scale Observatories: A Review. *Vadose Zone J.* **2008**, *7*, 358–389. [[CrossRef](#)]
43. Montzka, C.; Bogena, H.R.; Zreda, M.; Monerris, A.; Morrison, R.; Muddu, S.; Vereecken, H. Validation of Spaceborne and Modelled Surface Soil Moisture Products with Cosmic-Ray Neutron Probes. *Remote Sens.* **2017**, *9*, 103. [[CrossRef](#)]
44. UKSO. UK Soil Observatory Map Viewer: Soil Texture Layer. Available online: <https://mapapps2.bgs.ac.uk/ukso/home.html> (accessed on 20 June 2024).
45. U.S. Department of Agriculture. *Soil Survey Manual—Soil Survey Division Staff; Soil Conservation Service Volume Handbook*; United States Department of Agriculture: Washington, DC, USA, 2017; Volume 18.
46. Sentinel Online. Level-1 GRD Products. 2023. Available online: <https://sentinels.copernicus.eu/web/sentinel/technical-guides/sentinel-1-sar/products-algorithms/level-1-algorithms/ground-range-detected> (accessed on 1 September 2023).
47. Holmes, M. Applications of Radar in Agriculture. In *Applications of Remote Sensing in Agriculture*; Steven, M., Clark, J., Eds.; Butterworths: London, UK, 1990; pp. 307–330.
48. Copernicus Global Land Service. Normalized Difference Vegetation Index. 2023. Available online: <https://land.copernicus.eu/global/products/ndvi> (accessed on 1 September 2023).
49. Maslanka, W.; Morrison, K.; White, K.; Verhoef, A.; Clark, J. Retrieval of Sub-Kilometric Relative Surface Soil Moisture with Sentinel-1 Utilizing Different Backscatter Normalization Factors. *IEEE Trans. Geosci. Remote Sens.* **2022**, *60*, 4410613. [[CrossRef](#)]
50. Dobson, M.C.; Ulaby, F.T.; Hallikainen, M.T.; El-Rayes, M.A. Microwave Dielectric Behavior of Wet Soil-Part II: Dielectric Mixing Models. *IEEE Trans. Geosci. Remote Sens.* **1985**, *23*, 35–46. [[CrossRef](#)]
51. Natural England. *Natural England Technical Information Note TIN037*; Natural England: York, UK, 2008.

Disclaimer/Publisher's Note: The statements, opinions and data contained in all publications are solely those of the individual author(s) and contributor(s) and not of MDPI and/or the editor(s). MDPI and/or the editor(s) disclaim responsibility for any injury to people or property resulting from any ideas, methods, instructions or products referred to in the content.